Richness dependence of the recent evolution of clusters of galaxies

Manolis Plionis,[1,2]★ Hrant M. Tovmassian[2] and Heinz Andernach[3]†

[1]*National Observatory of Athens, Lofos Koufou, P. Penteli 152 36, Athens, Greece*
[2]*Instituto Nacional de Astrofísica Óptica y Electrónica, AP 51 y 216, 72000 Puebla, Pue, Mexico*
[3]*Argelander Inst. für Astronomie, Universität Bonn, D-53121 Bonn, Germany*

ABSTRACT

We revisit the issue of the recent dynamical evolution of clusters of galaxies using a sample of Abell, Corwin & Olowin (ACO) clusters with $z < 0.14$, which has been selected such that it does not contain clusters with multiple velocity components nor strongly merging or interacting clusters, as revealed in X-rays. We use as proxies of the cluster dynamical state the projected cluster ellipticity, velocity dispersion and X-ray luminosity. We find indications for a recent dynamical evolution of this cluster population, which however strongly depends on the cluster richness. Poor clusters appear to be undergoing their primary phase of virialization, with their ellipticity increasing with redshift with a rate $d\epsilon/dz \simeq 2.5 \pm 0.4$, while the richest clusters show an ellipticity evolution in the opposite direction (with $d\epsilon/dz \simeq -1.2 \pm 0.1$), which could be due to secondary infall. When taking into account sampling effects due to the magnitude-limited nature of the ACO cluster catalogue we find no significant evolution of the cluster X-ray luminosity, while the velocity dispersion increases with decreasing redshift, independent of the cluster richness, at a rate $d\sigma_v/dz \simeq -1700 \pm 400\,\mathrm{km\,s^{-1}}$.

Key words: galaxies: clusters: general – galaxies: evolution.

1 INTRODUCTION

Structure formation in cold dark matter (CDM) models proceeds by hierarchical anisotropic accretion of smaller units into larger ones, along filamentary large-scale structures (e.g. Zeldovich 1970; Blumenthal et al. 1984; Shandarin & Klypin 1984). The largest gravitationally bound, or nearly so, cosmic objects are clusters of galaxies, for which indeed, there are indications supporting their formation by hierarchical aggregation of smaller systems along filaments (e.g. West, Jones & Forman 1995; Plionis & Basilakos 2002). Since the perturbation growth rate depends on different cosmological models and the dark matter content of the Universe (e.g. Peebles 1980; Lahav et al. 1991), the present dynamical state of clusters of galaxies and its rate of evolution contains important cosmological information (e.g. Richstone, Loeb & Turner 1992; Evrard et al. 1993; Mohr et al. 1995; Suwa et al. 2003; Ho, Bahcall & Bode 2006).

A variety of recent studies have attempted to characterize the morphological and dynamical state of groups and clusters using either optical or X-ray data (Buote & Tsai 1995, 1996; Kolokotronis et al. 2001; Jeltema et al. 2005; Hashimoto et al. 2007, and references therein) and thus to infer the evidence for their cosmological evolution (e.g. Melott, Chambers & Miller 2001; Plionis 2002;

Jeltema et al. 2005; Rahman et al. 2006; Hashimoto et al. 2007). We can divide the various studies in those that have looked for indications of evolution at relatively high redshifts (e.g. Jeltema et al. 2005; Hashimoto et al. 2007) and those that have looked for a very recent evolution (Melott et al. 2001; Plionis 2002; Rahman et al. 2006). In both types of studies there appear contradictory results on whether the dynamical state of clusters evolves significantly in the distant or recent past. Melott et al. (2001) and Plionis (2002), using the projected ellipticity, ϵ, as a proxy of the cluster dynamical state (e.g. Kolokotronis et al. 2001), found a strong recent evolution rate with $d\epsilon/dz \simeq 0.7$–1 for $z \lesssim 0.15$. This appears to be in contradiction with a similar analysis for $z < 0.31$ of Rahman et al. (2006) and with numerical N-body simulations (e.g. Floor et al. 2003; Floor, Melott & Motl 2004; Ho, Bahcall & Bode 2006) that find the recent evolution of cluster ellipticity to be much weaker.

Clusters of high projected ellipticity are apparently still aggregating smaller groups and field galaxies from their surroundings. The increase of mass concentration and phase mixing during virialization will tend to sphericalize the clusters, increase their velocity dispersion, X-ray luminosity and temperature. Of course this simple picture is highly distorted by a variety of factors like the violent merging phase, strong interactions with a dense environment, cluster richness, interloper contamination, projection effects etc. For example, the analysis of numerical simulations by Jeltema et al. (2008) shows that, using morphological criteria, less than 50 per cent of clusters appearing relaxed in projection are truly relaxed.

★E-mail: mplionis@astro.noa.gr
†On leave of absence from Univ. Guanajuato, Mexico.

Therefore, in our present work we attempt to avoid systematic effects, as much as possible, by (a) selecting a cluster sample that is free of merging or strongly interacting clusters, (b) analysing the subsample of clusters which are free of sampling effects related to the magnitude limit of the Abell, Corwin & Olowin (ACO) parent cluster catalogue and (c) analysing separately clusters of different richness. We will use as proxies of the cluster dynamical state its projected flatness [f: related to the usually used ellipticity by $f = 1/(1 - \epsilon)$], X-ray temperature (kT_x) and luminosity (L_x), as well as velocity dispersion (σ_v). Of course, projection effects cannot easily be corrected for, a fact which will tend to hide or reduce the amplitude of the possible correlations we are seeking between cluster dynamical state and redshift.

2 DATA

For the purpose of this work we use the Abell, Corwin & Olowin (1989, hereafter ACO) clusters for which there are available velocity dispersion, ellipticity and X-ray temperature or luminosity measurements. Furthermore, we wish to concentrate mostly on the relatively slowly evolving clusters, via internal virialization processes, and make our analysis less prone to the complicated effects related to the dynamics of highly non-relaxed clusters, i.e. those in the state of merging, or those with multiple components, which could be interacting strongly with their surroundings. Note that we have chosen to use the ACO cluster catalogue because of the extensive multiwavelength studies of the individual ACO clusters and of the quality of the relevant data, which allows us to identify (and exclude) merging and strongly interacting clusters and be confident regarding the reality or not of each of the clusters. This is not yet possible, at the same level, with the new Sloan Digital Sky Survey (SDSS) or 2dF based cluster catalogues, since individual cluster multiwavelength studies of these samples are not yet available (at least for the majority of the clusters).

To produce a 'clean', of merging and interacting clusters, sample we used an updated version of a compilation of cluster redshifts and velocity dispersions (Andernach et al. 2005), which exploits all the available literature on galaxy redshifts to compile lists of galaxies in the direction of ACO clusters, and within a factor of 4 of the cluster's photometric redshift estimate. The 2007 version of the compilation is based on data from over 900 references and has ∼5500 cluster components for over 4000 different ACO clusters (3140 A- and 870 S-clusters), as well as a list of ∼110 000 individual member redshifts in 3750 different ACO clusters.

Since our final sample strongly depends on the definition of a single component cluster in this list, we present some details regarding the identification of different cluster components. The cluster velocity dispersion has been calculated by searching initially for any relative maxima in the redshift distribution within the cluster area. All galaxies within ±2500 km s^{-1} (i.e. just over three times the average σ_v of ∼700 km s^{-1}) around each relative maximum are included into a single cluster component. Subclumps of the same cluster which are closely located along the line of sight but with less than 2500 km s^{-1} separation in velocity were separated into different subclusters. Similarly, we register as different subclusters those with a smaller velocity separation which were reported in the literature as separated in the plane of the sky. The velocity dispersion of the different clusters and subclusters was calculated, correcting for measurement errors and relativistic effects, according to the prescriptions of Danese, de Zotti & di Tullio (1980), i.e. $\sigma_v = \sqrt{(\sigma_{obs}^2 - \sigma_{err}^2)/(1 + z)}$, where σ_{err} is the root-mean-square (rms) of the velocity errors of individual galaxies, or an adopted

mean error if individual errors were not available. We consider clusters that have at least four measured galaxy redshifts, while cluster velocity dispersions are considered only for those clusters that have a minimum of 10 measured redshifts.

Since our primary proxy for the cluster dynamical state is the cluster flatness, f, we start out from the sample of 342 ACO clusters for which Struble & Ftaclas (1994) compiled flatnesses from the literature. For details on the determination of the cluster-projected shape we point the reader to the original paper. Furthermore, we use a subsample of ACO clusters that excludes those showing evidences of strong merging or significant spatial distortions. The reason is that for such clusters most proxies of their dynamical state, used in our analysis (velocity dispersion, projected ellipticity, X-ray temperature and luminosity), are ill defined. To this end we identify and exclude clusters that, according to Andernach et al. (2005), have multiple components in velocity space. Furthermore and based (among others) on the analyses of Ledlow et al. (2003), de Filippis, Schindler & Erben (2005), Hashimoto et al. (2007) and Leccardi & Molendi (2008), we also exclude clusters that show multiple X-ray peaks or significantly distorted X-ray images, possibly implying a merging cluster (e.g. A754, A1066, A1213, A1317, A1318, A1468, A1474, A1552, A1644, A1750, A2151, A2244, A2382, A2384, A2401, A2459, A2554, A3528, A3532) or for which there is evidence for significant contamination of the X-ray measurement from the central active galactic nucleus (AGN, e.g. A2069, A2597). We caution the reader that our exclusion criteria may not completely clean our sample of significantly distorted clusters. As a test of such a residual contamination of our sample, we repeat our analysis without excluding the previously mentioned distorted clusters, to find that now our results, though mostly unchanged, become less statistically significant. This indicates that the possibly remaining such clusters in our sample would act towards reducing the significance of the intrinsic correlations.

We also imposed a minimum of 20 on the Abell galaxy count, N_A, which is the number of galaxies brighter than $m_3 + 2$, taken from ACO. The reason is that the ACO authors, different from Abell (1958), used a universal luminosity function to correct for the background galaxies, which led to most S-clusters having $N_A < 30$, as well as some A-clusters in the overlap zone (table 6 of ACO).

With the above restrictions we are left with 150 clusters (including one S-cluster) with $z < 0.14$, $N_A > 20$, and with measured shape parameters. Of these 140, 126 and 44 have velocity dispersion, X-ray luminosity and X-ray temperature measurements, respectively. The X-ray data have been taken from the X-Rays Clusters Database (BAX) (webast.ast.obs-mip.fr/bax; Sadat et al. 2004) which offers X-ray luminosities based on $H_0 = 50$ km s^{-1} Mpc^{-1} and $\Omega_m = 1.0$. For three clusters the BAX redshift differed by more than 5 per cent from our (more up-to-date) redshift, so we multiplied the X-ray luminosity in BAX with the factor $(z_{cl}/z_{BAX})^2$, where z_{cl} is the redshift from Andernach et al. (2005). The cluster sample used is presented in Table 1.

In the left-hand panel of Fig. 1 we present the redshift distribution of the cluster sample that we will analyse in this work (hashed histogram). The sample has a mean redshift of $\langle z \rangle \simeq 0.072$. However, since we wish to disentangle our analysis from effects related to the variable sampling of clusters of different richness at different redshifts, we divide our cluster sample into subsamples of different richness.

In the right-hand panel of Fig. 1 we plot the redshift distributions of clusters in three richness classes ($20 < N_A < 50$, $50 \leq N_A < 80$ and $N_A \geq 80$). We see that the poorer sample ($N_A < 50$) has a

Table 1. The Abell cluster sample used.

ACO	N_A	z_{LG}	N_z	σ_v (km s^{-1})	f	$L_x{}^a$ (10^{44} erg s^{-1})	kT_x (keV)
A13	96	0.0946	39	867	1.18	2.26	6.0
A14	29	0.0653	46	636	1.44	0.277	
A16	86	0.0843	7		1.25	0.900	
A21	56	0.0955	15	855	1.67	2.64	
A23	45	0.1067	29	454	2.32		
A27	46	0.0536	14	344	1.97		
A76	42	0.0407	13	459	1.47	0.490	1.50
A77	50	0.0717	4		1.79	1.74	
A84	76	0.1013	9		1.30	1.83	
A95	52	0.1095	23	511	1.61		
A112	50	0.1385	28	793	2.12	17.1^b	
A114	30	0.0582	43	888	1.55	0.158	
A119	69	0.0449	239	685	1.50	3.30	5.69
A126	51	0.0547	14	516	2.81	0.054	
A147	32	0.0444	31	720	1.22	0.391	
A150	55	0.0591	17	674	1.34	0.213	
A193	58	0.0490	75	708	1.56	1.53	
A195	32	0.0434	13	509	1.28	0.194	
A260	51	0.0367	51	518	1.40	0.199	
A272	52	0.0883	17	715	2.40	1.85	
A367	101	0.0899	33	900	1.20	1.20	
A376	36	0.0485	79	757	1.27	1.50	
A389	133	0.1131	55	759	1.21	1.55	
A399	57	0.0729	170	1101	1.42	7.06	6.46
A400	58	0.0242	125	683	1.48	0.706	2.15
A401	90	0.0735	170	1083	1.37	12.1	7.19
A415	67	0.0808	12	617	1.15	1.18	
A426	88	0.0186	190	1158	1.59	15.3	6.42
A496	50	0.0326	358	673	1.15	3.31	3.13
A505	39	0.0555	4		1.64	1.23	
A539	50	0.0290	159	699	1.25	1.10	3.04
A568	36	0.0761	5		1.56	0.460	
A655	142	0.1272	61	729	1.22	4.39	
A724	61	0.0924	72	474	1.53		
A727	65	0.0959	63	517	1.56		
A779	32	0.0228	81	339	1.38	0.083	2.97
A838	40	0.0515	11	421	2.15	0.091	
A858	44	0.0876	40	727	1.04	0.539	
A879	61	0.1116	35	754	1.20		
A979	39	0.0527	18	434	2.33	0.064	
A999	33	0.0314	51	374	1.66	0.056	
A1016	37	0.0317	46	221	1.78	0.067	
A1033	96	0.1227	38	739	1.22	5.12	
A1060	39	0.0117	330	696	1.24	0.461^b	3.15
A1100	35	0.0462	4		1.39	0.092	
A1139	36	0.0389	152	427	1.31	0.256	
A1149	34	0.0714	49	313	1.74		
A1168	52	0.0908	46	597	1.45		
A1169	73	0.0590	106	687	1.43	0.119	
A1173	52	0.0758	56	571	1.51	0.937	
A1187	55	0.0749	16	1049	2.24	0.093	
A1190	87	0.0755	23	809	1.34	1.75	
A1205	63	0.0753	76	762	1.86	1.77	
A1225	43	0.1037	56	780	2.00	6.23	
A1235	122	0.1042	4		2.00	1.70	
A1270	40	0.0691	57	556	1.69	0.113	
A1307	71	0.0805	97	794	1.34	7.43	

Table 1 – *continued*

ACO	N_A	z_{LG}	N_z	σ_v (km s^{-1})	f	$L_x{}^a$ (10^{44} erg s^{-1})	kT_x (keV)
A1314	44	0.0333	107	661	1.65	0.506	5.00
A1324	58	0.0946	12	241	1.36		
A1341	56	0.1049	28	432	1.36	0.153	
A1344	51	0.0765	7		1.25		
A1346	59	0.0979	97	732	2.03	0.371	
A1364	74	0.1058	64	527	1.33	0.071	
A1367	117	0.0220	283	756	1.52	1.25	3.55
A1371	55	0.0682	73	534	2.10	0.416	
A1377	59	0.0521	78	680	1.51	0.540	
A1380	76	0.1057	38	733	1.11		
A1383	54	0.0600	78	409	1.34	0.260	
A1407	56	0.1352	27	578	1.56	0.730	
A1412	86	0.1082	11	721	1.40	1.72^b	
A1424	52	0.0753	98	732	1.82	0.866	
A1436	69	0.0654	79	642	1.98	0.322	
A1448	70	0.1273	15	619	1.45	2.54	
A1452	46	0.0628	26	410	1.63		
A1496	58	0.0970	75	596	3.55	0.059	
A1520	45	0.0686	11	308	1.77	0.825	
A1541	58	0.0894	77	755	2.00	0.854	
A1620	42	0.0842	107	773	1.74	0.0036	
A1630	54	0.0648	34	440	1.61	0.100	
A1650	114	0.0836	220	789	1.46	6.05	5.68
A1651	70	0.0842	228	864	2.05	6.92	6.22
A1656	106	0.0233	794	948	1.58	7.77	8.25
A1668	54	0.0638	48	586	1.37	1.71	
A1691	64	0.0722	111	843	1.42	0.889	
A1738	85	0.1173	59	546	1.40		
A1764	42	0.1196	12	414	1.64	0.656	
A1767	65	0.0713	159	878	1.58	2.43	4.10
A1783	47	0.0688	57	369	1.33	0.364	
A1784	74	0.1262	12	414	2.93		
A1795	115	0.0625	127	782	1.39	10.3	5.22
A1800	40	0.0755	91	723	1.55	2.85	
A1827	68	0.0657	10	250	1.54		
A1828	59	0.0627	6		1.49		
A1837	50	0.0694	50	601	1.78	1.15	4.20
A1890	37	0.0574	93	515	1.19	0.623	5.77
A1904	83	0.0722	137	734	1.55	0.798	
A1913	53	0.0530	17	631	1.62	0.628	2.78
A1927	50	0.0952	50	650	1.16	2.30	
A1930	60	0.1318	16	352	1.78	3.99	
A1986	67	0.1165	12	798	1.59	1.73	
A1991	60	0.0589	65	665	1.80	1.42	2.71
A2022	50	0.0582	26	417	1.44	0.591	
A2026	51	0.0908	60	762	1.20	0.253	
A2048	75	0.0984	74	912	1.33		
A2052	41	0.0353	92	636	1.54	2.52	2.89
A2062	69	0.1126	57	646	1.33		
A2065	109	0.0724	42	968	1.32	5.55	5.37
A2089	70	0.0731	78	862	1.72	2.07	
A2092	55	0.0670	44	668	1.78	0.440	
A2107	51	0.0416	90	613	1.25	1.41	4.00
A2110	54	0.0978	46	477	1.84	3.70	
A2124	50	0.0667	118	787	1.22	1.66	4.41
A2142	89	0.0906	240	985	1.58	21.2	8.10
A2147	52	0.0353	93	821	2.03	2.87	4.34
A2148	41	0.0885	47	489	1.42	1.33	

Table 1 – *continued*

ACO	N_A	z_{LG}	N_z	σ_v (km s^{-1})	f	$L_x{}^a$ (10^{44} erg s^{-1})	kT_x (keV)
A2175	61	0.0965	84	768	1.91	2.84	
A2199	88	0.0311	471	714	1.64	4.09	3.97
A2244	89	0.0999	116	1116	1.16	7.13	5.77
A2245	63	0.0870	73	604	1.60	0.915	
A2247	35	0.0398	22	338	2.00		
A2250	52	0.0654	18	693	1.46	0.569	
A2255	102	0.0811	213	1145	1.25	4.43	5.92
A2256	88	0.0608	329	1159	1.73	7.40	6.98
A2372	42	0.0600	7		1.44	0.242	
A2377	94	0.0828	20	711	1.40	1.99	
A2410	54	0.0814	15	599	1.26	1.63	
A2415	40	0.0572	12	717	1.17	2.04	
A2420	88	0.0852	11	712	1.55	4.64	6.0
A2448	36	0.0823	43	455	1.69	0.052	
A2457	53	0.0595	34	492	1.22	1.25	
A2529	81	0.1084	25	940	1.54		
A2569	56	0.0811	42	501	1.58		
A2589	40	0.0419	70	797	1.24	1.90	3.38
A2597	43	0.0833	45	707	2.27	6.62^c	3.67^c
A2634	52	0.0317	254	1006	1.24	1.02	3.45
A2637	60	0.0713	11	579	1.33	1.50	
A2657	51	0.0407	76	728	1.42	1.75	3.53
A2666	34	0.0281	79	646	1.47	0.031	
A2670	142	0.0766	265	871	1.32	2.28	3.80
A2686	61	0.0530	4		1.31		
A2700	59	0.0949	9		1.55	1.50	
A2877	30	0.0251	170	1026	1.10	0.42	3.50
A3266	91	0.0586	317	1131	1.49	7.22	7.72
A3376	42	0.0455	113	759	1.75	1.78	4.43
A3395	54	0.0500	185	952	1.56	2.54	4.80
A3571	126	0.0386	171	896	1.56	7.51	6.80
A3667	85	0.0552	231	1102	1.59	9.16	6.28
A3716	66	0.0455	216	827	1.48	1.06	
A4059	66	0.0475	45	628	1.78	2.98	3.94
S463	26	0.0401	99	621	1.31		

$^a H_0 = 50$ km s^{-1} Mpc^{-1} is used.

$^b L_x$ corrected by a factor $(z_{cl}/z_{BAX})^2$.

$^c L_x$ and kT_x not used due to a possible significant central AGN contamination (McNamara et al. 2001; Morris & Fabian 2005).

redshift distribution significantly different from the richer sample ($N_A \geq 80$), with mean redshifts of 0.059 and 0.078, respectively.

Three of the four proxies that we use for the cluster dynamical state, namely the cluster velocity dispersion, X-ray luminosity and temperature, should be related to the total cluster mass based on the virial theorem and assuming hydrostatic equilibrium. Indeed, we find these parameters to be strongly correlated: the L_x–kT_x, L_x–σ_v and kT_x–σ_v Pearson correlation coefficients are $R = 0.75, 0.55, 0.65$, respectively, with random probabilities $\mathcal{P} < 10^{-5}$. Furthermore, we conjecture that cluster richness, as indicated by N_A, is proportional to the cluster total mass. We test this usual assumption by correlating the velocity dispersion and X-ray luminosities of the clusters of our sample with N_A. It is well known that the cluster X-ray luminosity is well correlated with the Abell cluster richness (e.g. Bahcall 1977; Johnson et al. 1983; Briel & Henry 1993; David, Forman & Jones 1999; Ledlow et al. 2003), and we confirm this also for our particular subsample of the ACO catalogue. Correlating N_A with σ_v and L_x we find the expected strong and significant correlations, which are shown in Fig. 2, with Pearson correlation coefficients of $R = 0.46$
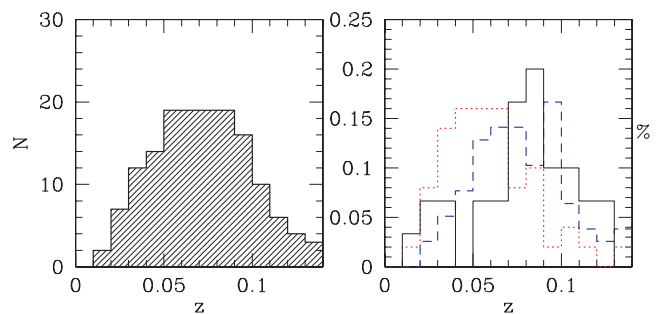
Figure 1. Left-hand panel: the redshift distribution of our cluster sample. Right-hand panel: the normalized redshift distribution of three subsamples based on different cluster richness. Clusters with $20 < N_A < 50$, $50 \leq N_A < 80$ and $N_A \geq 80$ are represented by the dotted, dashed and continuous line histograms, respectively.
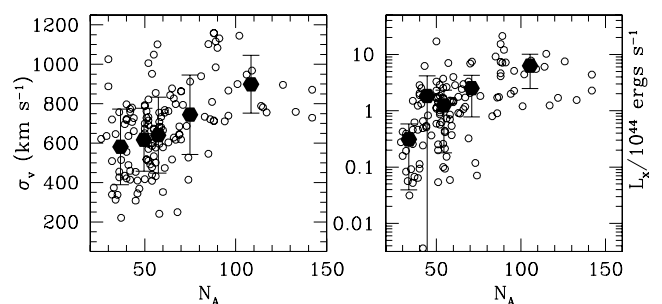
Figure 2. The correlation between Abell galaxy count, N_A, and the cluster velocity dispersion (left-hand panel) and X-ray luminosity (right-hand panel) for our sample. The filled symbols correspond to the mean values in bins of N_A and uncertainties are 1σ.

and 0.53, respectively, and corresponding random probabilities of $\mathcal{P} < 10^{-8}$.

3 RESULTS

We revisit the issue of the morphological and dynamical evolution of clusters in the recent past (see Melott et al. 2001; Plionis 2002) using as relevant indicators the four proxies mentioned previously. Note that the cosmic time, within the concordance cosmological model, corresponding to the redshift interval $0 < z < 0.14$ is ~1.73 Gyr, which is almost twice the cluster dynamical time-scale. However, we would like to stress that seeking indications of cluster evolution in relatively short time-scales can be hampered by many effects among which the intrinsic scatter of cluster shapes, the admixture of clusters of different formation times and of different richness, projection effects etc. As one example, we would like to point out that the rate of cluster ellipticity evolution should depend on cluster richness, since in principle massive structures will virialize faster than poorer ones of the same formation time. It is therefore imperative to analyse samples of different richness separately, and we do so further below.

As a first step, we present in Fig. 3 the correlations between redshift and the four proxies of the cluster dynamical state for the whole cluster sample. The continuous lines correspond to a least-squares fit to the unbinned data, and the filled symbols correspond to the mean values in redshift bins. We find a positive correlation, albeit quite weak, as in previous works. Specifically, we find Pearson correlation coefficients of $R = 0.12 \pm 0.02, 0.20 \pm 0.02$ and
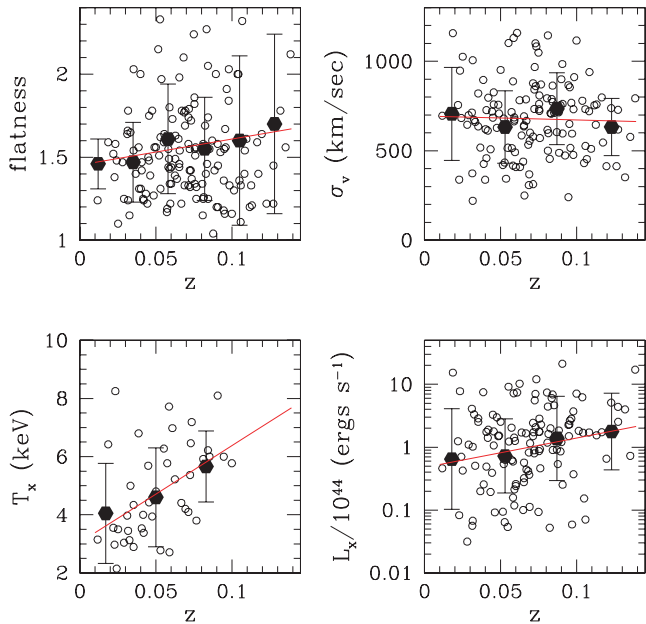
Figure 3. The apparent dependence on redshift of the cluster flatness, of the cluster velocity dispersion, of the ICM temperature and X-ray luminosity for our cluster sample. The line corresponds to the best least-square fit to the data while the filled symbols to the mean values in redshift bins and uncertainties are 1σ. However, both the L_x–z and strong kT_x–z correlations are found to be due to sample biases (see Section 3.1).

Figure 4. The dependence on redshift of the cluster absolute magnitude (based on the 10th brightest cluster member). In order to minimize sampling effects, related to the magnitude-limited nature of the ACO cluster sample, we investigate clusters in the reduced ('volume-limited') area delineated by the continuous lines.

0.46 ± 0.03 for the f–z, L_x–z and kT_x–z correlations, respectively, with corresponding probabilities of being chance correlations of $\mathcal{P} = 0.08, 0.015$ and 0.0008. The correlation coefficient uncertainties are estimated by a procedure by which we exclude randomly, 100 times, 10 per cent of the clusters and re-estimate the correlation coefficient, R, from each reduced sample.

3.1 Accounting for systematic biases

In general, using magnitude-limited cluster catalogues, one should be aware of the effects of sampling different cluster richnesses at different redshifts, *effects which could act to either weaken, enhance or even create apparent redshift-dependent correlations*. Although the ACO cluster catalogue, as shown by a number of studies, is roughly volume limited within $z \lesssim 0.1$ (but mostly the $R \geq 1$ richness class cluster subsample) it is essential to investigate whether sampling biases could be disguised as 'evolutionary' trends. For example, as shown by analyses of cosmological simulations, richer clusters which correspond to more massive dark matter haloes are expected to be on average more elongated than poorer ones (e.g. Jing & Suto 2002; Kasun & Evrard 2005; Allgood et al. 2006; Gottlöber & Turchaninov 2006; Paz et al. 2006; Bett et al. 2007; Macció et al. 2007; Ragone-Figueroa & Plionis 2007). Therefore, the fact that at higher redshifts the sampled clusters could be typically richer than the lower redshift counterparts (as expected in flux or magnitude-limited samples), implies that we could observe an artificial correlation due to exactly the magnitude-limited nature of the sample. Similarly, the fact that the X-ray luminosity is correlated with the cluster richness implies that the average cluster L_x at higher redshifts could well appear to be larger than the corresponding value at lower redshifts.

Furthermore, an important sample incompleteness bias could also be present in the published X-ray temperatures, since X-ray spectro-

scopic measurements would be more easily available for the most X-ray brightest rather than fainter high-z clusters and therefore the apparently strong evolutionary trend of kT_x could well be due to this bias. Further below we test for this effect.
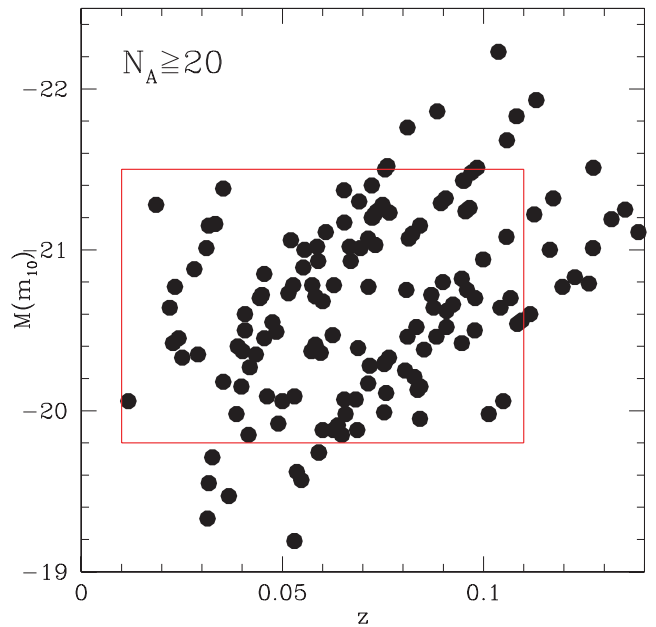
We now investigate the possible influence of the magnitude-limited nature of the parent ACO cluster sample by confining our analysis within a range of absolute magnitudes (based on the 10th brightest cluster member) for which there appears to be no systematic redshift-dependent sampling effects. In Fig. 4 we present the cluster m_{10}-based absolute magnitude as a function of redshift for our sample. We can indeed observe the usual redshift-dependent trend which is caused by the magnitude-limited nature of the sample. We now use only those clusters that fall within the 'volume-limited' area, delineated by continuous lines ($-21.5 < M < -19.8$ and $z \leq 0.11$), for which no systematic redshift-dependent trend is observed. We find that only the originally observed L_x–z correlation disappears, a fact that implies that this correlation is artificial and related to the variable sampling of different cluster richness at different redshifts. However, the f–z and kT_x–z correlations remain as significant as for the whole sample ($R = 0.16 \pm 0.02$ and 0.42 ± 0.03, respectively, with corresponding probabilities of being chance correlations of $\mathcal{P} = 0.05$ and 0.003), while the former correlation (f–z) appears to be even slightly stronger (although still weak in an absolute sense).

The observed f–z correlation corresponds to a cluster ellipticity evolution rate of

$$d\epsilon/dz \simeq 0.95 \pm 0.18,$$

with ϵ the projected ellipticity, which is in good agreement with the Automated Plate Measurement (APM) cluster results ($d\epsilon/dz \simeq 0.7$) of Plionis (2002) and the study of optical and X-ray cluster results ($d\epsilon/dz \simeq 1$) of Melott et al. (2001). However, the results of Flin, Krywult & Biernacka (2004), based on Abell clusters and analysed by Rahman et al. (2006), yield a significantly lower rate

of cluster ellipticity evolution, $d\epsilon/dz \simeq 0.26$. It is interesting that *N*-body simulations also show a recent evolution of the ellipticity of simulated clusters, but the rate of evolution is quite low (e.g. Floor et al. 2004; Rahman et al. 2006).

We now test whether the strong kT_x–z correlation could be due to the incompleteness bias, discussed previously. To this end we compare the L_x–z correlation of those clusters that have kT_x measurements with that of the overall sample of clusters with L_x data. We indeed find that the former subsample has a strong and significant L_x–z correlation ($R = 0.44 \pm 0.03$ with $\mathcal{P} = 0.002$), while the parent sample shows no significant L_x–z correlation ($R = 0.05$). This proves that indeed the overall kT_x–z correlation is artificial and due to incompleteness. Therefore, no more reference will be given to kT_x-based results.

3.2 Correlations as a function of cluster richness

In an attempt to reconcile the different evolutionary rates of cluster ellipticity, found in different studies, one should keep in mind the possible influence of sampling different cluster richnesses at different redshifts (due to the magnitude-limited nature of the samples and of volume effects). Furthermore, if clusters of different richness evolve at different rates, then in comparing observations with simulations one should make sure to match the cluster richness (mass) distribution of the samples compared. It is therefore clear that the comparison of cluster samples with a different mix of poor and rich clusters at different redshifts are susceptible to interpretational error.

We therefore analyse independently the different richness subsamples and we indeed find not only varying amplitudes but also opposite slopes of these correlations. From now on we will present results based only on the restricted ('volume-limited') subsample of our original cluster sample.

In order to highlight the richness-dependent differences, we present below results based on the poorest and richest cluster subsamples. For clarity we present in Fig. 5 the selected region in the absolute magnitude–redshift plane for the different richness subsamples.

The Pearson correlation coefficients for the different correlations and richness subsamples are shown in Table 2. We find the f–z correlations for the poorest and the richest cluster subsamples to have opposite signs. They also show higher absolute amplitudes than in the full cluster sample. We also find a σ_v–z correlation, in all richness subsamples, which is washed out in the whole cluster sample (i.e. when we do not take into account the different cluster
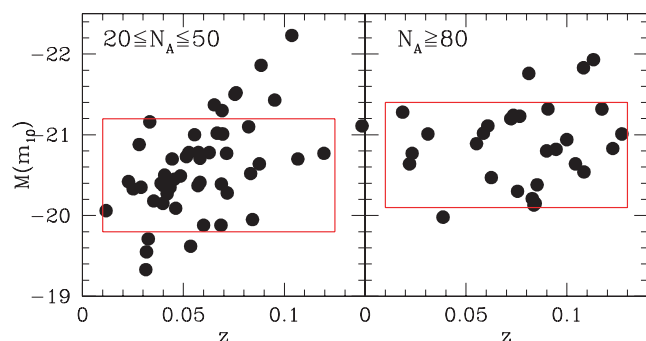
Table 2. Pearson correlation coefficients and their significance for the correlations with redshift of the three (unbiased) proxies of the cluster dynamical state. Results are based on the 'volume-limited' subsamples. We indicate the most significant correlations in bold font.

N_A	f–z			σ_v–z			L_x–z		
	#	R	P	#	R	P	#	R	P
>20	120	**0.17**	**0.03**	110	−0.05	0.30	103	0.06	0.3
20–50	38	**0.40**	**0.01**	34	**−0.22**	**0.10**	32	−0.05	0.4
51–79	45	0.06	0.40	44	**−0.29**	**0.03**	37	−0.06	0.4
≥80	26	**−0.38**	**0.03**	25	**−0.30**	**0.07**	24	−0.17	0.2
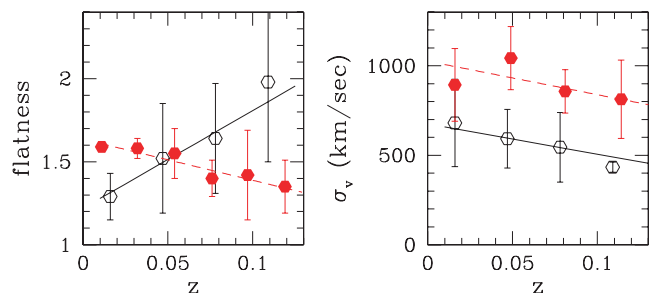
Figure 6. The redshift–flatness (left-hand panel) and redshift–velocity dispersion (right-hand panel) mean correlations for the poorest (open symbols and continuous lines) and the richest (solid symbols and dashed lines) cluster subsamples.

richness). Finally, we note again that we find no significant L_x–z correlation in any of the subsamples. In Fig. 6 we present only the significant correlations, i.e. the redshift dependence of the cluster mean ellipticity (left-hand panel) and of the velocity dispersion (right-hand panel), binned in the redshift axis, for the poorest (open points and continuous line) and the richest (filled points and dashed line) samples, respectively.

It is important to note that the rate of ellipticity evolution for the poorer cluster subsample is larger than that of the whole cluster sample, with

$$d\epsilon/dz \simeq 2.4 \pm 0.4 \quad (20 \leq N_A \leq 50),$$

while the corresponding rate for the richest subsample is

$$d\epsilon/dz \simeq -1.2 \pm 0.1 \quad (N_A \geq 80),$$

which is opposite to the trend found for the poorest clusters, i.e. the cluster ellipticity increases with decreasing redshift.

In order to visualize better the effect of cluster richness on the sign and the strength of the correlations of the three (unbiased) proxies of the cluster dynamical status with redshift, we present in Fig. 7 (left-hand panels) both the Pearson and Spearman correlation coefficients, evaluated in the three richness bins. We remind the reader that positive or negative correlation coefficients indicate that, on average, the cluster parameter decreases or increases towards lower redshifts, respectively. In the right-hand panels of Fig. 7 we present a joint indication of the significance and strength of each correlation in the form of the ratio between the correlation coefficient, R, and the probability, $\mathcal{P}$, that it is a random correlation. Large values of this ratio (and definitely >1) indicate relatively strong and significant correlations. Different line styles and symbols in Fig. 7 correspond to the different cluster parameters (see figure caption). Correlation coefficient uncertainties are again estimated

Figure 5. The dependence on redshift of the cluster absolute magnitude (based on the 10th brightest cluster member) for the richest and poorest cluster sample. The reduced ('volume-limited') area used in the richness-dependent analysis is delineated by the continuous lines.
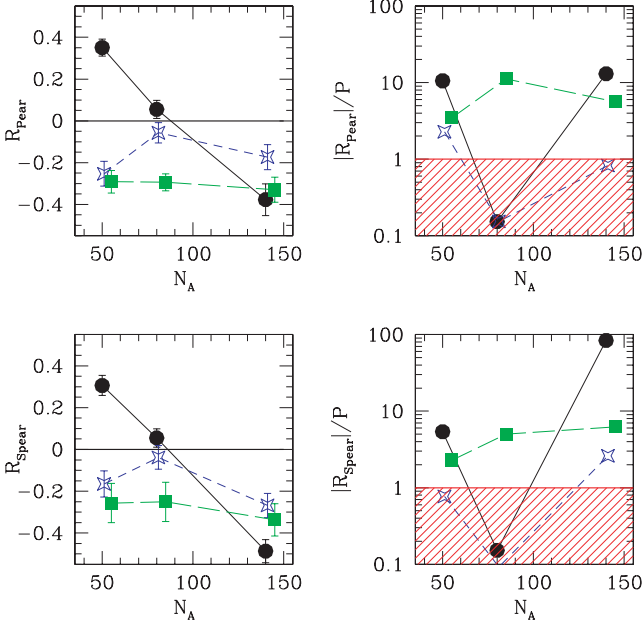
Figure 7. The correlation coefficients (left-hand panels) and a measure of their significance (right-hand panels) as a function of cluster richness (upper panels: Pearson; lower panels: Spearman). The three (mostly) unaffected by incompleteness proxies are shown: f–z (black solid line, solid circles), L_x–z (blue short-dashed line, squares) and σ_v–z (green long-dashed line, solid squares), as a function of Abell count, N_A. In the right-hand panels we present an indication of significance of the correlations with those having low values of $R/\mathcal{P}$ being not significant. The shaded region corresponds to $R/\mathcal{P} \lesssim 1$.

according to the procedure described earlier. The main results are following.

(i) We find indications, of varying significance, for a recent evolution of two out of the three (unbiased) proxies of the cluster dynamical state (flatness and velocity dispersion).

(ii) There is a change of the evolutionary behaviour of the cluster flatness as a function of richness. The correlation changes to anticorrelation going from poor to richer clusters. The intermediate richness subsample shows no f–z correlation and therefore there seems to be a smooth transition of the sign of the f–z correlation from the poorest to the richest clusters. The rate of ellipticity evolution for the poorest and richest cluster subsamples are $d\epsilon/dz \simeq 2.4$ and -1.2, respectively.

(iii) The most significant evolutionary trend is that of cluster flatness with the velocity dispersion following. The rate of the σ_v evolution is $d\sigma_v/dz \simeq -1700 \pm 400 \, \mathrm{km \, s^{-1}}$, independent of the richness.

3.3 Robustness tests

3.3.1 Does $d\epsilon/dz$ depend on limiting redshift?

In order to test whether the evolution rate of cluster flatness is sensitive to the sample limiting redshift, and thus to a few redshift outliers, we plot in the left-hand panel of Fig. 8 $|d\epsilon/dz|$ as a function of limiting sample redshift for the richest (filled points) and the poorest (open symbols) subsamples. The individual uncertainties are again estimated using a procedure by which we exclude randomly, 100 times, 10 per cent of the clusters and re-estimate $d\epsilon/dz$
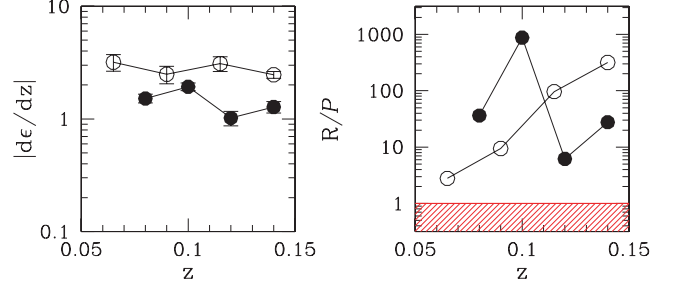
Figure 8. Left-hand panel: the dependence of the cluster ellipticity evolution rate on the limiting sample redshift. Filled and open points correspond to the richest and poorest samples, respectively. Note that since $d\epsilon/dz$ is negative for the richest subsample, we plot its absolute value. Right-hand panel: a measure of the corresponding significance of the estimated $d\epsilon/dz$ (see main text). Values corresponding to $R/\mathcal{P} \lesssim 1$ (shaded region) are not significant.

from each reduced sample. In the right-hand panel of Fig. 8 we also provide the $R/\mathcal{P}$ indication of significance of each measured $|d\epsilon/dz|$ value. As can be seen the amplitude of the evolutionary trend does not depend on the limiting redshift, while the significance of the correlation for the poorest cluster subsample, although still (relatively) strong, drops at lower redshifts, a fact which we attribute to the small number of available clusters.

3.3.2 Are the evolutionary trends due to mass-dependent systematic effects?

In order to demonstrate clearly that the observed evolutionary trends are not related to any residual cluster mass-dependent systematic effect, we plot in Fig. 9 the mean flatness, σ_v and L_x for two sets of well-separated redshift bins and as a function of richness, i.e. an analogue of Fig. 6 but as a function of N_A. If there was no real evolution, one should have expected to see a trend of all proxies with N_A (due to their dependence on cluster mass), but overlapping for
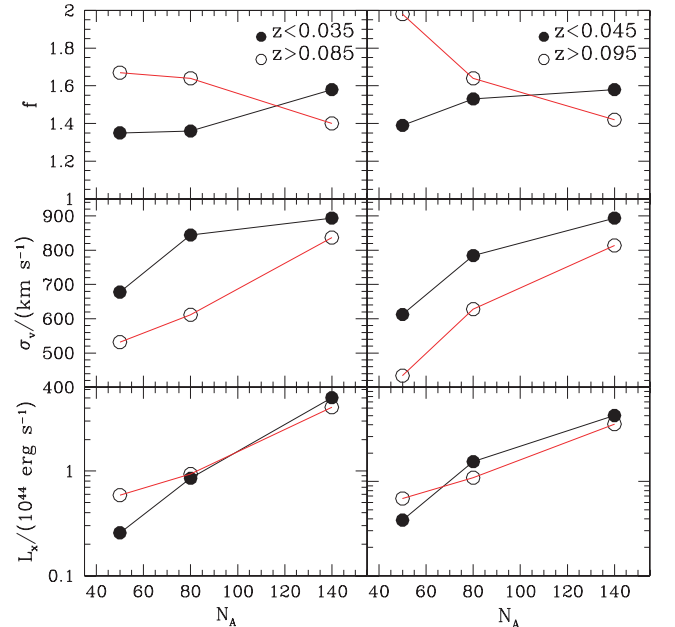
Figure 9. The variation with richness of the mean cluster dynamics proxies for two sets of well-separated redshift bins (indicated in the plot).

the lower and higher z subsamples. Alternatively, if the evolutionary trends are real we should see systematic, non-overlapping in z, offsets between the trends in different ranges of N_A. Indeed, as can be seen from Fig. 9, the only parameter of which the richness dependence overlaps in redshift is L_x, which however we have already correctly identified as non-evolving with redshift.

3.4 Possible interpretation

These results can be interpreted if the population of poorer clusters is dynamically younger than that of the richer ones, and that they are now going through their primary virialization process, which tends to sphericalize their original anisotropic morphologies.

Regarding the rich clusters, one could have interpreted the fact that their velocity dispersion increases at lower redshifts again as an indication of them becoming more virialized, since once the cluster potential has accumulated the bulk of the mass, via infall and merging, then the virialization processes will tend to increase the velocity dispersion. However, if this were the case then there should have been also signs of the clusters becoming more spherical at lower redshifts, which is exactly the opposite than what is observed. Therefore, the previous interpretation does not seem plausible. Rather it appears that the rich clusters of our sample have already reached a virialized state, while the redshift-dependent changes in their dynamical state (evidenced by the increase of their flatness and velocity dispersion) are probably caused by secondary infall (Gunn 1977; see also Ascasibar, Hoffman & Gottlöber 2007 and references therein; Diemand & Kuhlen 2008).

If on the other hand the poor cluster population is currently going through the primary virialization process, there should be a clear correlation between cluster flatness and velocity dispersion, as well as with intracluster medium (ICM) X-ray luminosity. Since we have taken good care to exclude multiple component and merging clusters, we believe that the velocity dispersion measurement is not significantly contaminated by the infall component of the merging process or by strong tidal effects and thus it should indeed reflect the cluster dark matter gravitational potential. Similarly, the ICM (traced by the X-ray luminosity) should not be significantly contaminated by effects related to shocks induced during the merging process and thus it should also reflect the dynamical state of our clusters.

We therefore correlate, for our poorest cluster subsample, cluster flatness with velocity dispersion and X-ray luminosity. Since we are not seeking evolutionary trends we do not impose limits in absolute magnitude. We find a strong and significant anticorrelation in the first two cases (Fig. 10). The Pearson correlation coefficients
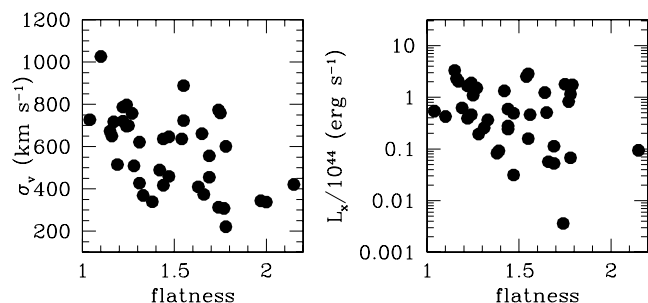
Figure 10. Correlation of two proxies for cluster dynamical state for the poorest subsample ($20 < N_A < 50$, $z < 0.1$). Left: the dependence of cluster velocity dispersion on cluster flatness. Right: the dependence of cluster X-ray luminosity on cluster flatness.

are $R = -0.43 \pm 0.03$ and -0.39 ± 0.03 for the $f - \sigma_v$ and $f - L_x$ correlations, respectively, with corresponding random probabilities of $\mathcal{P} = 3 \times 10^{-3}$ and 0.007. These results indeed show the expected behaviour for a cluster population at different stages of virialization. It is important to note that similar correlations are not found in the richer subsamples, as expected if these clusters are already virialized.

We conclude that poor and relatively nearby clusters are currently evolving dynamically and they appear to be at various stages of virialization. Richer clusters (at the redshift range probed) are probably already virialized, but show indications of being affected by secondary infall.

4 DISCUSSION AND CONCLUSIONS

Our current analysis supports previous results regarding the recent ($z \lesssim 0.14$) evolution of the ellipticity and dynamics of clusters of galaxies. We have found however that the direction of evolution is different for clusters of different richness. Regarding the rate of ellipticity evolution we find $d\epsilon/dz \simeq 0.95$ for our full cluster sample, which is in good agreement with Melott et al. (2001) and Plionis (2002), but in disagreement with Rahman et al. (2006) who quote a value $d\epsilon/dz \simeq 0.2$. It is important to note that the evolution rates for the poorest and richest of our clusters have opposite signs: $d\epsilon/dz \simeq 2.4 \pm 0.4$ and $d\epsilon/dz \simeq -1.2 \pm 0.1$, respectively. It is clear that the overall evolution rate of a sample of clusters depends on the richness mix, and this could well be the reason why different studies find different values of $d\epsilon/dz$.

Summarizing, we would like to point out the following:

(1) From the observational point of view, the relatively strong recent evolution of cluster ellipticity and dynamical state applies mostly to poor clusters, for which the rate of evolution ($d\epsilon/dz \simeq 2.4$) is significantly larger than that of the whole sample put together ($d\epsilon/dz \simeq 0.95$). Rich clusters appear to have reached an equilibrium state earlier and thus they do not show signs of positive evolution in the recent past, but rather of a negative evolution ($d\epsilon/dz \simeq -1.2$), possibly due to secondary infall (e.g. Gunn 1977; Ascasibar et al. 2007; Diemand & Kuhlen 2008). There are also indications for a recent evolution of the cluster velocity dispersion, increasing with decreasing redshift but apparently independent of the cluster richness, with a rate $d\sigma_v/dz \simeq -1700 \pm 400 \, \text{km s}^{-1}$. No evolution is observed of the ICM X-ray luminosity.

(2) The discrepancy with the ellipticity evolution results of Flin et al. (2004), analysed in Rahman et al. (2006), could well be due to the latter study not taking into account the cluster richness dependence of the effect, or due to not excluding strongly interacting and merging clusters and possibly also to the sample's larger limiting redshift ($z \lesssim 0.31$).

(3) The discrepancy with N-body results could be due to a number of reasons. A quite probable reason is related to the fact that the simulated clusters are predominantly rich (Floor et al. 2003, 2004) for which, as we have shown, there is no observational evidence for a recent positive evolution, but rather there are indications for a mild negative evolution. Rahman et al. (2006) simulated also poorer clusters, but the total number of analysed clusters is quite small ($N = 41$). Since the intrinsic scatter of cluster (and halo) shapes is large and the observed effect appears to be inherently weak, a large cluster sample is probably necessary in order to clearly establish the evolutionary effect. Furthermore, if the richness mix of the simulated clusters is significantly different from that of the observed clusters (or between different observational cluster samples), then due to the

richness dependence of the effect, one could derive different rates of evolution from different richness mixes.

REFERENCES

Abell G. O., 1958, ApJS, 3, 211
Abell G. O., Corwin H. G., Jr, Olowin R. P., 1989, ApJS, 70, 1 (ACO)
Allgood B. F., Flores A., Primack J. R., Kravtsov A. V., Wechsler R. H. F. A., Bullock J. S., 2006, MNRAS, 367, 1781
Andernach H., Tago E., Einasto M., Einasto J., Jaaniste J., 2005, in Fairall A. P., Woudt P., eds, ASP Conf. Ser. Vol. 329, Nearby Large-Scale Structures and the Zone of Avoidance. Astron. Soc. Pac., San Francisco, p. 283
Ascasibar Y., Hoffman Y., Gottlöber S., 2007, MNRAS, 376, 393
Bahcall N. A., 1977, ApJ, 217, L77
Bett P., Eke V., Frenk C. S., Jenkins A., Helly J., Navarro J., 2007, MNRAS, 376, 215
Blumenthal G. R., Faber S. M., Primack J. R., Rees M. J., 1984, Nat, 311, 517
Briel U. G., Henry J. P., 1993, A&A, 278, 379
Buote D. A., Tsai J. C., 1995, ApJ, 452, 522
Buote D. A., Tsai J. C., 1996, ApJ, 458, 27
Danese L., de Zotti G., di Tullio G., 1980, A&A, 82, 322
David L. P., Forman W., Jones C., 1999, ApJ, 519, 533
de Filippis E., Schindler S., Erben T., 2005, A&A, 444, 387
Diemand J., Kuhlen M., 2008, ApJ, 680, L25
Evrard A. E., Mohr J. J., Fabricant D. G., Geller M. J., 1993, ApJ, 419, L9
Flin P., Krywult J., Biernacka M., 2004, in Diaferio A., ed., IAU Colloq. 195, Outskirts of Galaxy Clusters: Intense Life in the Suburbs. Cambridge Univ. Press, Cambridge, p. 248
Floor S., Melott A. L., Miller C. J., Bryan G. L., 2003, ApJ, 591, 741
Floor S., Melott A. L., Motl P. M., 2004, ApJ, 611, 153
Gottlöber S., Turchaninov V., 2006, in EAS Publ. Ser. Vol. 20, p. 25
Gunn J. E., 1977, ApJ, 218, 592
Hashimoto Y., Böhringer H., Henry J. P., Hasinger G., Szokoly G., 2007, A&A, 467, 485
Ho S., Bahcall N., Bode P., 2006, ApJ, 647, 8
Jeltema T. E., Canizares C. R., Bautz M. W., Buote D. A., 2005, ApJ, 624, 606
Jeltema T. E., Hallman E. J., Burns J. O., Motl P. M., 2008, ApJ, 681, 167
Jing Y. P., Suto Y., 2002, ApJ, 574, 538
Johnson M. W., Cruddace R. G., Wood K. S., Ulmer M. P., Kowalski M. P., 1983, ApJ, 266, 425
Kasun S. F., Evrard A. E., 2005, ApJ, 629, 781
Kolokotronis E., Basilakos S., Plionis M., Georgantopoulos I., 2001, MNRAS, 320, 49
Lahav O., Rees M. J., Lilje P. B., Primack J. R., 1991, MNRAS, 251, 128
Leccardi A., Molendi S., 2008, A&A, 486, 359
Ledlow M. J., Voges W., Owen F. N., Burns J. O., 2003, AJ, 126, 2740
Macció A. V., Dutton A. A., van den Bosch F. C., Moore B., Potter D., Stadel J., 2007, MNRAS, 378, 55
McNamara B. R. et al., 2001, AJ, 562, L149
Melott A. L., Chambers S. W., Miller C. J., 2001, ApJ, 559, L75
Mohr J. J., Evrard A. E., Fabricant D. G., Geller M. J., 1995, ApJ, 477, 8
Morris R. G., Fabian A. C., 2005, MNRAS, 358, 585
Paz D. J., Lambas D. G., Padilla N., Merchán M., 2006, MNRAS, 366, 1503
Peebles P. J. E., 1980, The Large-Scale Structure of the Universe. Princeton Univ. Press, Princeton, NJ
Plionis M., 2002, ApJ, 572, L67
Plionis M., Basilakos S., 2002, MNRAS, 329, L47
Ragone-Figueroa C., Plionis M., 2007, MNRAS, 377, 1785
Rahman N., Krywult J., Motl P. M., Flin P., Shandarin S. F., 2006, MNRAS, 367, 838
Richstone D., Loeb A., Turner E. L., 1992, ApJ, 393, 477
Sadat R., Blanchard A., Kneib J.-P., Mathez G., Madore B., Mazzarella J. M., 2004, A&A, 424, 1097
Shandarin S. F., Klypin A., 1984, SvA, 28, 491
Struble M. F., Ftaclas C., 1994, AJ, 108, 1
Suwa T., Habe A., Yoshikowa K., Okamato T., 2003, ApJ, 588, 7
West M. J., Jones C., Forman W., 1995, ApJ, 451, L5
Zeldovich Ya. B., 1970, A&A, 5, 84

This paper has been typeset from a TeX/LaTeX file prepared by the author.